

---

Delft University of Technology

# Flow distribution analysis of the NACA 0012 airfoil at different angles of attack

*Delft University of Technology, Delft, South Holland, 2628 CD*

---

Andrea Bettini<sup>1</sup> 4656970  
Changkyu Park<sup>1</sup> 4646061  
Elrawy Soliman<sup>1</sup> 4684443  
Malte Wegener<sup>1</sup> 4672194

**Submission Date:** 2021-06-17  
**Course:** AE4180  
**Group:** 15  
**Supervisors:** Dr. A. Sciacchitano  
Prof.dr. F. Scarano

---

<sup>1</sup>Graduate Student, Faculty of Aerospace Engineering, Aerodynamics Department, Delft University of Technology,  
Kluyverweg 2, 2629 HS Delft

# Contents

<b>Contents</b>	<b>2</b>
<b>List of Figures</b>	<b>3</b>
<b>List of Tables</b>	<b>4</b>
<b>1 Introduction</b>	<b>5</b>
<b>2 Experimental Setup</b>	<b>6</b>
2.1 Wind tunnel . . . . .	6
2.2 HWA setup . . . . .	7
2.2.1 Measurement parameters . . . . .	8
2.3 Sampling rate determination . . . . .	10
2.4 PIV setup . . . . .	10
2.4.1 Measurement parameters . . . . .	11
<b>3 Results and Discussion</b>	<b>13</b>
3.1 HWA results . . . . .	13
3.1.1 Mean velocity profiles . . . . .	13
3.1.2 RMS . . . . .	14
3.2 PIV results . . . . .	15
3.2.1 Effect of window size . . . . .	15
3.2.2 50% overlap and 3 multipass iterations and comparison with the self-made code . . . . .	19
3.2.3 Velocity statistics . . . . .	20
3.3 Instantaneous and mean flow comparison . . . . .	25
3.4 Comparison of HWA and PIV . . . . .	26
<b>4 Conclusion</b>	<b>29</b>
<b>Works Cited</b>	<b>30</b>

# List of Figures

2-1	Test section of the W-tunnel installed with the model. Base image acquired from the student manual made by Sciacchitano et al. [1, Figure 1.] . . . . .	6
2-2	How wire measurement set up, image taken from Sciacchitano et al. [1, Figure 2.] . .	7
2-3	4-th order calibration curve . . . . .	9
2-4	Autocorrelation coefficient of the time series with different time lag values . . . . .	9
2-5	Droplet size distribution, taken from the works of Sciacchitano et al. [1, Figure 5.] . .	11
3-1	$U_{\text{mean}}, U'_{\text{RMS}}$ at different $\alpha$ . . . . .	14
3-2	20 <sup>th</sup> TIFF image of $\alpha = 0^\circ$ , $dt = 100 \mu\text{s}$ . . . . .	16
3-3	$\alpha = 0^\circ$ , 20 <sup>th</sup> quiver contour plot, $dt = 100 \mu\text{s}$ , interrogation window size = 64 pixels, 0% overlap, single pass . . . . .	16
3-4	$\alpha = 0^\circ$ , 20 <sup>th</sup> quiver contour plot, $dt = 100 \mu\text{s}$ , interrogation window size = 32 pixels, 0% overlap, single pass . . . . .	16
3-5	$\alpha = 0^\circ$ , 10 <sup>th</sup> quiver contour plot, $dt = 100 \mu\text{s}$ , interrogation window size = 16 pixels, 0% overlap, single pass . . . . .	16
3-6	20 <sup>th</sup> TIFF image of $\alpha = 5^\circ$ , $dt = 100 \mu\text{s}$ . . . . .	17
3-7	$\alpha = 5^\circ$ , 20 <sup>th</sup> quiver contour plot, $dt = 100 \mu\text{s}$ , interrogation window size = 64 pixels, 0% overlap, single pass . . . . .	17
3-8	$\alpha = 5^\circ$ , 20 <sup>th</sup> quiver contour plot, $dt = 100 \mu\text{s}$ , interrogation window size = 32 pixels, 0% overlap, single pass . . . . .	17
3-9	$\alpha = 5^\circ$ , 3 <sup>rd</sup> quiver contour plot, $dt = 100 \mu\text{s}$ , interrogation window size = 16 pixels, 0% overlap, single pass . . . . .	17
3-10	100 <sup>th</sup> TIFF image of $\alpha = 15^\circ$ , $dt = 100 \mu\text{s}$ . . . . .	18
3-11	$\alpha = 15^\circ$ , 100 <sup>th</sup> quiver contour plot, $dt = 100 \mu\text{s}$ , interrogation window size = 64 pixels, 0% overlap, single pass . . . . .	18
3-12	$\alpha = 15^\circ$ , 100 <sup>th</sup> quiver contour plot, $dt = 100 \mu\text{s}$ , interrogation window size = 32 pixels, 0% overlap, single pass . . . . .	18
3-13	$\alpha = 15^\circ$ , 9 <sup>th</sup> quiver contour plot, $dt = 100 \mu\text{s}$ , interrogation window size = 16 pixels, 0% overlap, single pass . . . . .	18
3-14	Comparison of PIV-results between the professional and self-made code for $\alpha = 0^\circ$ , 20 <sup>th</sup> quiver contour plot, $dt = 100 \mu\text{s}$ , interrogation window size = 32 pixels, 50% overlap . . . . .	19
3-15	Comparison of PIV-results between the professional and self-made code for $\alpha = 5^\circ$ , 20 <sup>th</sup> quiver contour plot, $dt = 100 \mu\text{s}$ , interrogation window size = 32 pixels, 50% overlap . . . . .	19
3-16	Comparison of PIV-results between the professional and self-made code for $\alpha = 15^\circ$ , 100 <sup>th</sup> quiver contour plot, $dt = 100 \mu\text{s}$ , interrogation window size = 32 pixels, 50% overlap . . . . .	20
3-17	Comparison of PIV-results between the professional and self-made code for $\alpha = 15^\circ$ , 20 <sup>th</sup> quiver contour plot, $dt = 6 \mu\text{s}$ , interrogation window size = 32 pixels, 50% overlap . . . . .	20

3-18 Velocity plots of $\alpha = 0^\circ$ , $dt = 100 \mu\text{s}$ , interrogation window size = 32 pixels, 50% overlap, triple pass . . . . .	21
3-19 Velocity plots of $\alpha = 5^\circ$ , $dt = 100 \mu\text{s}$ , interrogation window size = 32 pixels, 50% overlap, triple pass . . . . .	21
3-20 Velocity plots of $\alpha = 15^\circ$ , $dt = 100 \mu\text{s}$ , interrogation window size = 32 pixels, 50% overlap, triple pass, 100 samples . . . . .	22
3-21 Velocity plots of $\alpha = 15^\circ$ , $dt = 100 \mu\text{s}$ , interrogation window size = 32 pixels, 50% overlap, triple pass, 10 samples . . . . .	22
3-22 Velocity plots of $\alpha = 15^\circ$ , $dt = 6 \mu\text{s}$ , interrogation window size = 32 pixels, 50% overlap, triple pass . . . . .	22
3-23 Velocity profile plots at $x/c = 1.2$ , interrogation window size = 32 pixels, 50% overlap, triple pass . . . . .	24
3-24 HWA and PIV comparison of $U_{\text{mean}}$ and $U'_{\text{RMS}}, V'_{\text{RMS}}$ at different $\alpha$ . . . . .	27

## List of Tables

2-1 Voltage-velocity calibration coefficients . . . . .	9
---	---

# 1 Introduction

The use of numerical tools to determine the flow field distribution around a shape of interest is often limited by the complexity of the numerical model utilized and user knowledge on the tools used. As such, it is vital to compare and validate numerical outputs with experimental data, in particular towards the latter parts of design processes. This report details the flow distribution around a NACA-0012 airfoil at different angles of attack. In order to do so, hot wire anemometry (HWA) and particle image velocimetry (PIV) measurements are conducted. These measurements are post-processed using written scripts, and are compared against each other.

Due to the limitations of onsite experimentation for the 2020-2021 experimental campaign, experimental data has been provided by the aerodynamics department of TU Delft.

# 2 Experimental Setup

This chapter details the experimental setup used. The wind tunnel is described, and both the HWA and PIV setup are given alongside their measurement parameters.

## 2.1 Wind tunnel

All information in this section is paraphrased from the student manual made by Sciacchitano et al. [1]. The experimental data released for the lab exercise was gathered using the W-tunnel at the High Speed Laboratory, situated at Delft University of Technology. The tunnel is an open, low speed wind tunnel, where air is driven into the tunnel's inlet by an electrically-powered (16.5 kW) centrifugal fan. The inlet of the tunnel consists of a plenum with dimensions  $2.0 \times 1.5 \times 2.0 \text{ m}^3$  ( $L \times W \times H$ ) and it is followed by a diffuser. The diffuser decelerates the airflow into a settling chamber with two gauzes, where the gauzes reduce the turbulence intensity. A contraction then reaccelerates the flow into a nozzle, from which the air is blown into the open room (via a duct). The nozzle exit has a cross-section of  $0.40 \times 0.40 \text{ m}^2$ . The flow is uniform in the central region of  $0.32 \times 0.32 \text{ m}^2$ , with root-mean-squared (RMS) fluctuations in the  $x$ -velocity component of  $< 0.2\%$  of the free-stream velocity (based on Laser Doppler Anemometer measurements at  $10.2 \text{ m s}^{-1}$ ) [2, 3]. An image of the wind tunnel's test section with the experimental setup is given in Fig. 2-1.

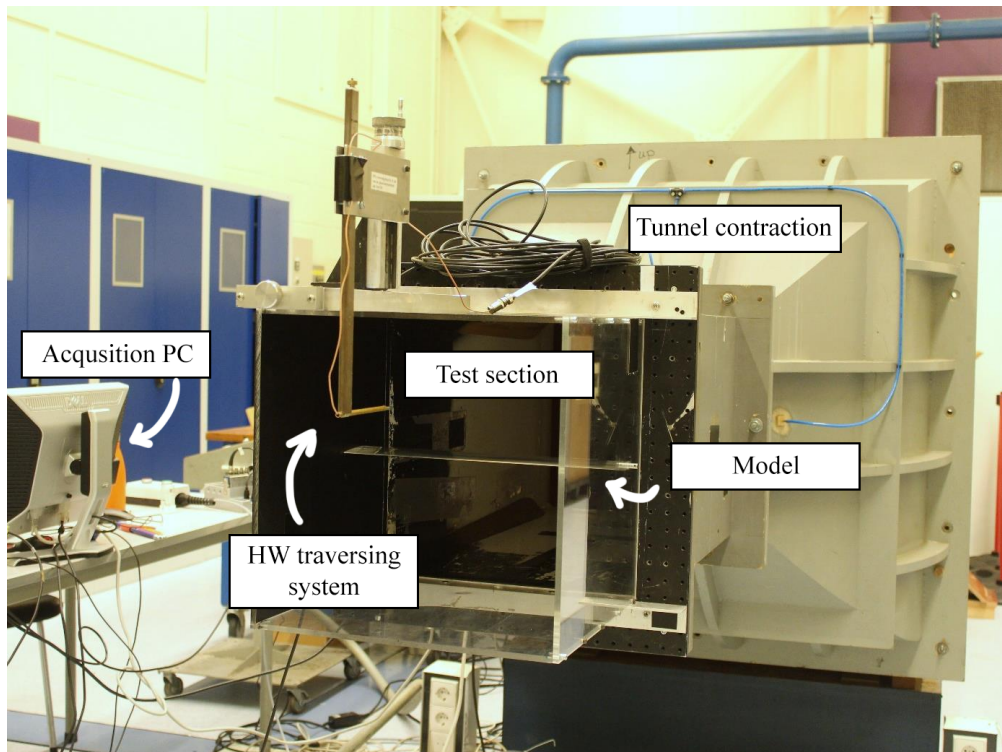


**FIGURE 2-1** Test section of the W-tunnel installed with the model. Base image acquired from the student manual made by Sciacchitano et al. [1, Figure 1.]

It should be noted that the wind tunnel experimental setup did not use a pitot-static probe to measure the wind tunnel velocity as onsite experimental measurements were not conducted<sup>1</sup>. In principle, a pitot-static probe is equipped with a total pressure port and static pressure port, which are used to measure the total pressure and static pressure respectively. The difference between the two measurements is the dynamic pressure, which is used to calculate the (mean) tunnel velocity. The pitot-static probe is positioned sufficiently upstream of the model / test-section to get an estimate of the tunnel velocity. It should also be noted that the pitot-static probe effectively measures the squared velocity, which does not allow decomposition of the velocity into a mean flow component and fluctuation velocity components, hence the calculation is an approximation of the mean tunnel velocity.

**Airfoil selection** A Plexiglas NACA-0012 airfoil with a chord length of 100 mm is installed in the test section for this experiment. It spans the full width of the test section and rotates around the quarter-chord point.

## 2.2 HWA setup

The setup used to generate the HWA data consists of a hot wire probe, a constant temperature anemometer bridge, and a data acquisition system. All information is extracted from the works of Sciacchitano et al. [1]. The system integration is given in Fig. 2-2.

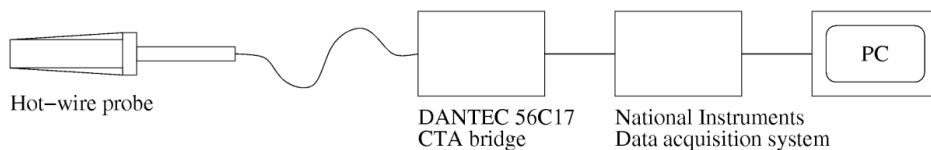


FIGURE 2-2 How wire measurement set up, image taken from Sciacchitano et al. [1, Figure 2.]

**Hot wire probe** The probe used is a  $5\text{ }\mu\text{m}$  platinum-plated tungsten wire directly welded to prongs. The wire acts as the sensor of the system.

**Constant temperature anemometer bridge** The *Dantec 56C17 CTA bridge* is the control circuit for HWA. It is a Wheatstone bridge where one of the four electrical resistors is the sensor. The bridge can be also used as a resistance-measuring device to set the correct overheat ratio.

**Data acquisition system** Analog voltage measurements are acquired using a *National Instruments BNC-2110* block connector connected to a *NI PCI-6024E* data acquisition board. The acquisition board turns the analog voltage to a digital voltage. LABVIEW is used to read and display the voltage output from the bridge.

<sup>1</sup>AE4180 (2020/2021): *Lecture 10 - Live lab session from wind tunnel* [1:48:30 / 1:52:45] [last accessed 2021-05-27]

### 2.2.1 Measurement parameters

The primary concern within this assignment is that experimental data was obtained from a primary source. As such, the design calculations are deduced rather than calculated. These deductions come directly from the work of Sciacchitano et al. [1] and the calibration data provided.

**Velocity calibration** In this section, the velocity calibration is discussed, and the calibration curve is presented. To perform the calibration, the cold resistance of the system need to be determined first. Then, the overheat ratio is selected which enables the calculation of the hot resistance. The total resistance consists of the resistance of the cable, the wire and the two supports. To find this resistance, the Wheatstone bridge is balanced first with the system connected. Balancing the Wheatstone bridge refers to having a zero voltage by changing one of the Wheatstone bridge resistances. To have a zero voltage,  $R_x$  is changed to obtain an equal ratio between the resistances as follows:

$$\frac{R_x}{R_{\text{total},c}} = \frac{R_A}{R_B}. \quad (2-1)$$

where  $R_{\text{total},c}$  is the cold resistance of the total system,  $R_A$  and  $R_B$  are known resistances, and  $R_x$  is the resistance that is varied to achieve the equality given in Eq. 2-1.

Once the Wheatstone bridge is balanced, the system is disconnected while the CTA adapter is connected and the resistance of the system that was connected earlier  $R_{\text{total},c}$  is shortcut. The new voltage is measured, which is used to determine the total resistance cold of the system  $R_{\text{tot},c}$ . Similar procedures are applied to determine the cold resistance of the cable. The only difference is that the CTA adapter is set to  $5\Omega$  instead of shortcut. This is because the system is not capable of measuring small resistances, so the added  $5\Omega$  allows for a more accurate measurement. The resistance of the cable is then found by subtracting this  $5\Omega$  from the obtained resistance. Since the resistance of the support is provided by the manufacturer as  $R_{\text{probe lead}} = 0.5\Omega$  and the cable and the total resistance are measured, the wire resistance is computed as follows:

$$R_{\text{wire},c} = R_{\text{total},c} - (R_{\text{cable}} + R_{\text{probe lead}}).$$

**Overheat ratio** The overheat ratio  $a$  describes the resistance of the hot wire probe when heated in comparison to its resistance at ambient temperature. Effectively, it describes the sensitivity of the probe, with high values allowing for small flow fluctuations to be picked up (as the resistance change is high). For the experiment, it was decided that  $a = 0.5$  [1]. This number comes without justification, but is easily justified as the result of a trade-off between being able to measure flow fluctuations (i.e. not having a too low  $a$ ) and not having the probe burn out (i.e. not having a too high  $a$ ). The overheat ratio is given by

$$a = \frac{R_{w,\text{hot}} - R_{w,\text{cold}}}{R_{w,\text{cold}}}.$$

Since the cold resistance of the wire  $R_{\text{probe}}$  and the overheat ratio are known, the hot wire resistance can be computed. Based on the resistance of the system, the voltage can then be measured given that the current is known.

**Calibration curve** The voltage was measured for different known velocities at a constant wire temperature and a constant flow temperature. To obtain the relation between the voltage and velocity, 11 measurements of different velocities ranging between  $0 \text{ m s}^{-1}$  and  $20 \text{ m s}^{-1}$  at increments of  $2 \text{ m s}^{-1}$  were obtained. The relation between the measured voltage and the velocity is governed by King's law, which reads

$$E^2 = A + BU^n.$$

The calibration coefficients  $A$ ,  $B$ , and  $n$  need to be found to obtain the relation between the measured voltage and the velocity. To obtain the velocity  $U$  as a function of the voltage  $E$ , a 4<sup>th</sup>-order polynomial is fitted to the calibration data as  $n \approx 0.5$ . The 4<sup>th</sup>-order polynomial has the form:

$$U = C_0 + C_1E + C_2E^2 + C_3E^3 + C_4E^4. \quad (2-2)$$

To ensure that there is a one-to-one relation between the measured voltage and the velocity,  $C_1$  was set to zero to obtain a zero gradient of velocity with respect to the voltage at  $U = 0 \text{ m s}^{-1}$ . By ensuring that  $dU/dE|_{U=0} = 0 \text{ m s}^{-1} \text{ V}^{-1}$ , then at  $U = 0 \text{ m s}^{-1}$ , there is only one corresponding voltage  $E$ .

The voltage was measured at a sampling rate of 2 kHz for 5 s for the aforementioned velocities. The average of each of the voltage measurements was computed and the calibration coefficients in Eq. 2-2 were obtained using the known velocities. The calibration curve is shown in Fig. 2-3 with the calibration coefficients presented in Tab. 2-1.

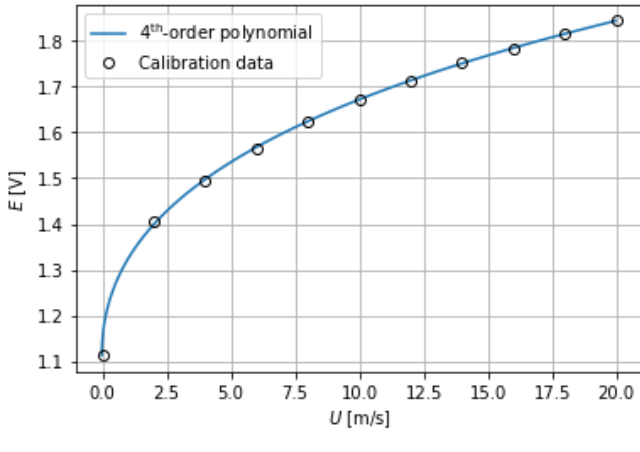


FIGURE 2-3 4-th order calibration curve

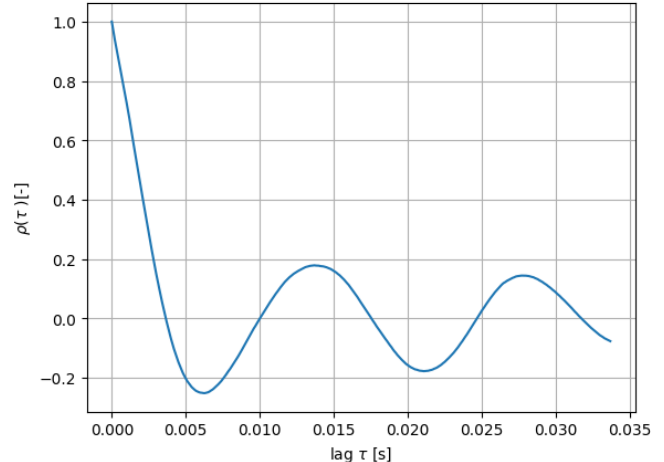


FIGURE 2-4 Autocorrelation coefficient of the time series with different time lag values

TABLE 2-1 Voltage-velocity calibration coefficients

$C_0$	$C_1$	$C_2$	$C_3$	$C_4$
-0.0203254	0	18.6424	18.8097	9.73747

## 2.3 Sampling rate determination

The sampling rate is chosen such that it guarantees that the samples are not correlated. This ensures that the obtained time series consists of independent and identically distributed time samples. Since the autocorrelation is a measure of how much a signal is correlated to its' shifted self, the autocorrelation is used to determine the appropriate sampling rate.

The normalized autocorrelation coefficient  $\rho_x$  is defined as the ratio between the correlation with a time shift  $\tau$  to the correlation with no time shift ( $\tau = 0$  s) as follows:

$$\rho_x(\tau) = \frac{R_x(\tau)}{R_x(0)}, \quad (2-3)$$

where  $R_x(\tau)$  is the correlation with a shift  $\tau$  and  $R_x(0)$  is the correlation with no time shift. To make sure that the time series signal is not correlated, an estimate of the sampling rate (SR) is made using the condition that

$$\text{SR} \leq \frac{1}{2T_I}, \quad (2-4)$$

where  $T_I$  is the integral time scale. The integral time scale is the time shift that results in a zero normalized auto-correlation coefficient. To obtain  $T_I$ , different time shifts (lags) were used until a zero normalized autocorrelation was obtained. These time shifts are based on a shift in the discrete time series, where a discrete time shift corresponds to a shift of one index in the discrete time series. The discrete shift was then transformed to a continuous time lag using the sampling rate by dividing the discrete shift by the used sampling rate (10 kHz). This result in an integral time scale  $T_I = 0.0037$  s. The result of calculating the normalized autocorrelation coefficient of the time series with different time lag values is shown in Fig. 2-4. The figure shows that  $\tau = T_I = 0.0037$  s results in a zero normalized autocorrelation coefficient as expected. Based on an integral time scale of  $T_I = 0.0037$  s, the sampling rate is computed using Eq. 2-4. This results in a maximum allowed sampling rate SR = 135.1 kHz.

## 2.4 PIV setup

The setup used to generate the PIV data consists of a seeding generator, laser, CCD camera, and a PIV acquisition software. All information is extracted from the works of Sciacchitano et al. [1].

**Seeding generator** The *SAFEX fog generator* is used to seed the tunnel with a non-toxic water-glycol based fog, produced from the *SAFEX normal power mix* fluid. The droplet size distribution has mean 1  $\mu\text{m}$  and is distributed with the shape given in Fig. 2-5.

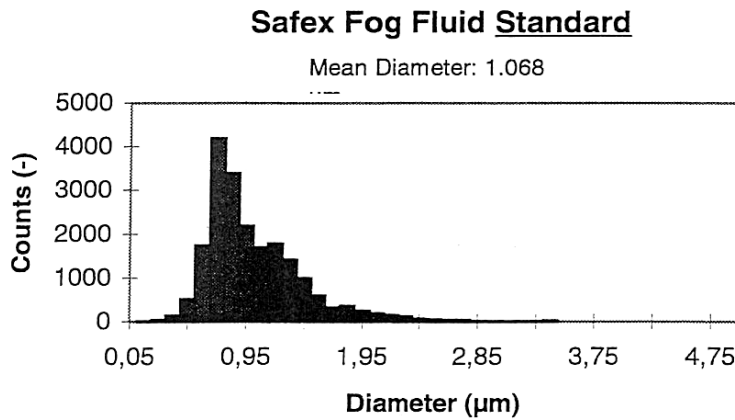


**FIGURE 2-5** Droplet size distribution, taken from the works of Sciacchitano et al. [1, Figure 5.]

**Laser** The *Quantel Evergreen 200* laser is utilized. The laser system is a double pulsed Nd:YAG laser producing infrared light of wavelength 1064 nm. A second harmonic generator halves the wavelength to 532 nm. At maximum power, the energy in each laser pulse is 200 mJ. Each pulse is 8 ns long and the maximum repetition rate is 15 Hz for each pulse, and the beam diameter is 6 mm.

**CCD camera** The *Bobcat IMPERX IGV-B1610* CCD camera is used to record the PIV images. The CCD has a resolution of  $1628 \times 1236$  pixels with  $4.40 \mu\text{m}$  pixel pitch and 10-bit black and white images. The camera exposure is controlled such that the first exposure has a duration of  $10 \mu\text{s}$  and the second exposure has a duration of 100 ms. To control the imaging of the particles onto the camera sensor, a Nikon  $f = 35 \text{ mm}$  lens is used, and the ratio between the lens focal length and aperture  $f_{\#}$  can be set from 2.8 to 32.

**PIV acquisition software** Image acquisition and analysis is done through DaVis. DaVis is responsible for illumination and acquisition control, image analysis, data post processing, and data display and output. More information can be found in the student manual of Sciacchitano et al. [1].

### 2.4.1 Measurement parameters

It was aforementioned that the primary concern within this assignment is that experimental data was obtained from a primary source. As such, the design calculations are deduced rather than calculated. From the provided calibration airfoil image, it is noted that the ratio between the image size and one of the 10 mm intervals within the image  $K$  is calculated as

$$K = \frac{\text{total horizontal \#pixels}}{\#\text{pixels associated to interval}} \approx 16.477,$$

where the denominator for  $K$  is  $\approx 98.8$  pixels. As such, the FOV, expressed as the horizontal distance captured in the camera's image, is

$$\text{FOV} = KX \approx 164.77 \text{ mm},$$

where the sheet interval length  $X$  is already known to be 10 mm. The magnification factor is then straightforwardly calculated as

$$M = \frac{\text{pixel size} \times \text{number of pixels in the sensor}}{\text{FOV}} \approx 0.04348, \quad (2-5)$$

where the pixel size is 4.4  $\mu\text{m}$  from the camera specifications. Based on the magnification factor and the thin lens equation

$$M = \frac{d_i}{d_o}, \quad \frac{1}{f} = \frac{1}{d_i} + \frac{1}{d_o},$$

it is possible rewrite the thin lens equation as

$$\frac{1}{f} = \frac{1}{d_o} \left( 1 + \frac{1}{M} \right).$$

Therefore the object distance (between object and lens)  $d_o$  is

$$d_o = f \left( 1 + \frac{1}{M} \right) \approx 840.0 \text{ mm},$$

and the image distance (between image and lens)  $d_i$  is

$$d_i = M d_o \approx 36.5 \text{ mm}.$$

To consider the  $f_{\#}$  of the system, both the particle image diameter and depth of field criteria are considered. The particle image diameter criterion states that the optimal particle diameter after considering light diffraction is between 2 and 3 pixels, i.e.

$$d_{\text{diff}} = 2.44\lambda f_{\#}(1 - M) \approx 2 \text{ pixels} - 3 \text{ pixels},$$

where  $\lambda$  is the laser light wavelength. This leads to the following range for  $f_{\#}$ :

$$f_{\#} = \frac{d_{\text{diff}}}{2.44\lambda(1 - M)} \approx 7.087 - 10.631.$$

To check whether light diffraction is the limiting criterion for  $f_{\#}$ , we note that the depth of field  $\delta z$  as a function of  $f_{\#}$  is given as

$$\delta z = 4.88\lambda f_{\#}^2 \left( 1 + \frac{1}{M} \right)^2 \approx 75.1 \text{ mm} - 169.0 \text{ mm}.$$

Considering that the laser sheet thickness  $\Delta z \approx 2 \text{ mm}$ , then  $\Delta z \ll \delta z$ , so the choice of  $f_{\#}$  is limited by light diffraction<sup>2</sup>.

Finally, based on the experimental data parameters,  $\Delta t = 6 \mu\text{s}$  and  $\Delta t = 100 \mu\text{s}$ . Do note that in general,  $\Delta t$  is limited such that particles are displaced at maximum 25% of the interrogation window or 25% of the laser sheet thickness.

---

<sup>2</sup>AE4180 (2020/2021): *Laser sheet thickness*

[last accessed 2021-06-16]

# 3 Results and Discussion

This chapter details the  $x/c = 1.2$  velocity profiles obtained with both HWA and PIV. Additionally, the PIV velocity contours are visualized and discussed.

## 3.1 HWA results

With HWA, both the mean  $x$ -velocity  $U_{\text{mean}}$  and root-mean-square  $x$ -velocity fluctuations  $U'_{\text{RMS}}$  are obtained. A brief discussion on the obtained results is provided in this section.

### 3.1.1 Mean velocity profiles

After processing the calibration data and obtaining the calibration coefficients, the data for the different angles of attack was processed. The voltage measurements were averaged and the velocities were obtained using the calibration coefficients. Figure 3-1a, Fig. 3-1c, and Fig. 3-1e show the mean velocity for the angles of attack  $\alpha = 0^\circ$ ,  $10^\circ$ , and  $15^\circ$ , respectively. There exists low measured velocities close to  $y = 0$  mm as a result of the probes being in the wake of the airfoil. As  $y$  increases, the velocity magnitudes increase as the probe is being moved out of the wake.

The velocity profiles depend on the angle of attack due to the change in the wake shape. It is noted that increasing the angle of attack increases the wake size. That is, for larger  $\alpha$ , the velocities are reduced up to larger  $y$  values (away from the center of the wake), which indicates that the wake and its influence are more significant. At  $\alpha = 15^\circ$ , the reduction in velocity is much larger than the other two angles of attack where the velocity was reduced to  $\approx 3 \text{ m s}^{-1}$  for  $\alpha = 15^\circ$ . This indicates a possible leading edge separation which is expected at such large angles of attack.

Another observation is the increase in velocity to values larger than  $10 \text{ m s}^{-1}$  out of the wake. This is due to the wake blockage effect since the wind tunnel used is with a closed test section. The wake blockage refers to the increase in the velocity out of the wake due to the presence of the wake. The mass flow has to remain constant, therefore the decrease in the velocity in the wake is compensated by the increase in velocity out of the wake. The velocity out of the wake is larger for larger angles of attack due to smaller velocities in the wake for larger angles of attack.

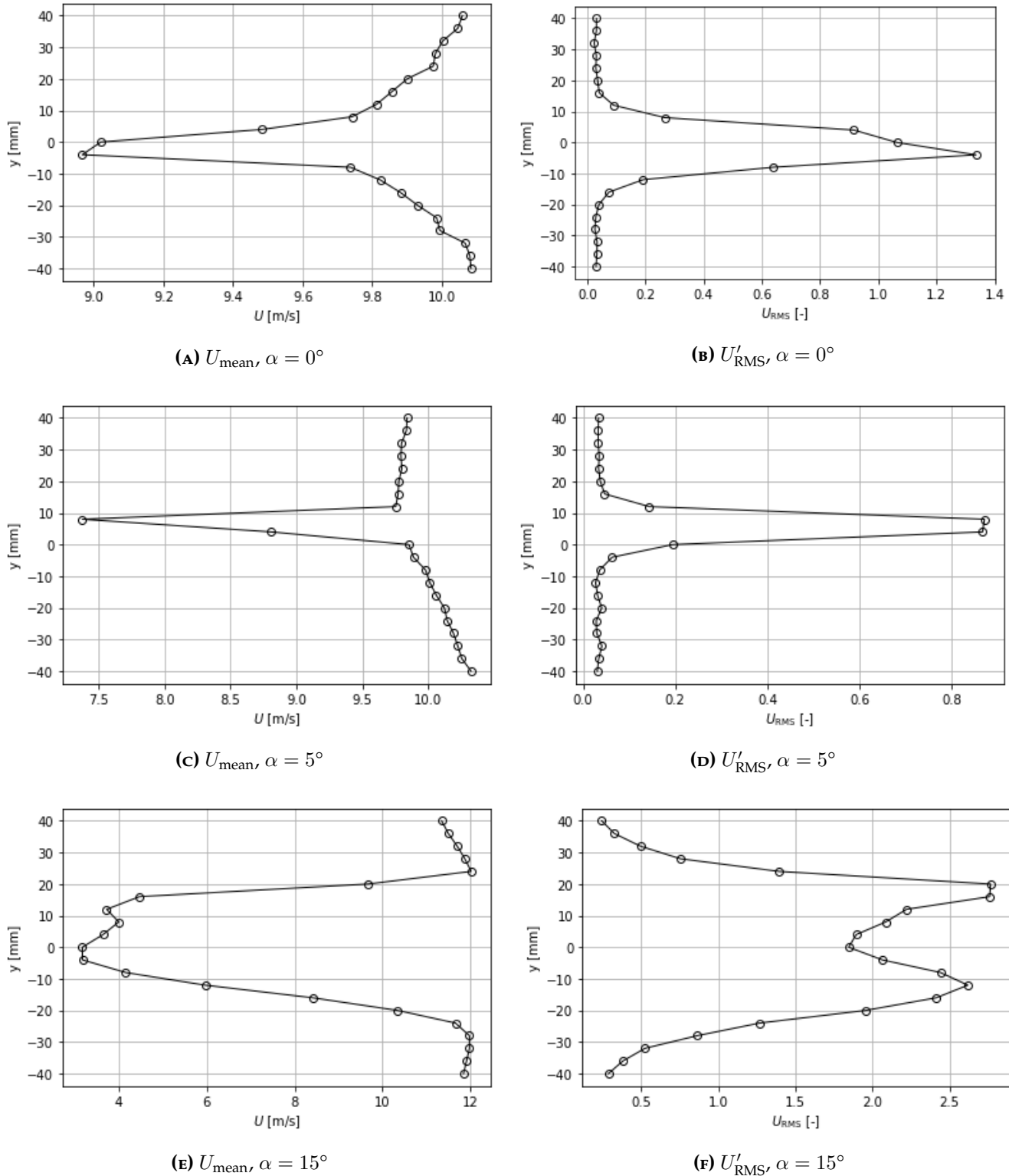


FIGURE 3-1  $U_{\text{mean}}, U'_{\text{RMS}}$  at different  $\alpha$

### 3.1.2 RMS

In this section, the root-mean-square velocity profiles are presented for the different angles of attack. At each  $y$  location, the RMS velocity is computed by calculating the difference between

the measured velocity and the mean of the corresponding measurement as follows:

$$U'_{\text{RMS}} = \sqrt{\frac{1}{N-1} \sum_{i=1}^N (U_i - U_{\text{mean}})^2} \quad (3-1)$$

As shown in Eq. 3-1, the RMS velocity is a measure for the spread of the velocity around the mean velocity of the flow. Therefore, a larger RMS velocity indicates larger fluctuations and disturbances in the flow. The root-mean-square velocity was computed for at  $x/c = 1.2$  for  $\alpha = 0^\circ, 10^\circ$ , and  $15^\circ$  and the result are shown in Fig. 3-1b, Fig. 3-1d, and Fig. 3-1f.

The RMS velocity is larger in the wake region as expected since the wake region is unsteady. Since the wake region gets larger as the angle of attack increases, the RMS velocity is larger up until larger  $y$  values at larger angles of attack. That is, the region with high fluctuations is larger for larger angles of attack due to a larger wake region. Looking at Fig. 3-1f, the region with highly unsteady flow is the largest compared to the other angles of attack. This is expected as a result of the flow separation at  $\alpha = 15^\circ$  as explained in Sec. 3.1.1.

## 3.2 PIV results

In this section, the parameters for the PIV analysis software are determined. Furthermore the instantaneous velocity fields are compared between the professional and self-made code and the Reynolds-averaged flowfields are presented.

**Setting up MATLAB** In order to begin the cross-correlation process of image pairs and produce relevant plots for further analyses, the `Determine_Magnification.m` MATLAB file is used to determine values of a few parameters such as the magnification factor and the coordinates of the origin. These values are then transferred over to `WIDIMtif_Main.m`. This file is the main MATLAB file that outputs required velocity data and contour plots that are presented later in the report. Firstly, the magnification factor was found to be 0.04295 which validates the value obtained using Eq. 2-5 within 2% difference. The origin was also retrieved from the same file, being roughly at around  $(x, y) = (128, 530)$  pixels.

### 3.2.1 Effect of window size

The cross-correlation of image pairs were executed using three different window sizes: 64, 32 and 16 using the `WIDIMtif_Main.m` MATLAB file for the three values of angle of attack  $\alpha = 0^\circ, 5^\circ$  and  $15^\circ$  at  $dt = 100 \mu\text{s}$ , 0% overlap and single pass (`iterNum = 1`). It is to be noted that while 20 images were used for the cases of  $\alpha = 0^\circ$  and  $5^\circ$ , 100 images were used for  $\alpha = 15^\circ$ .

**$\alpha = 0^\circ$  analysis** Starting with  $\alpha = 0^\circ$  that has 20 images in total, the 20<sup>th</sup> TIFF image is presented in Fig. 3-2 to visualise the system under analysis. Using the 20 images, quiver contour plots have been produced for window sizes of 64, 32 and 16 pixels as shown in Fig. 3-3, Fig. 3-4 and Fig. 3-5 respectively. As for the window size of 16 pixels, it is to be noted that the MATLAB program could not execute beyond the 10<sup>th</sup> image, ultimately running into error, and thus the 10<sup>th</sup> image has been presented.

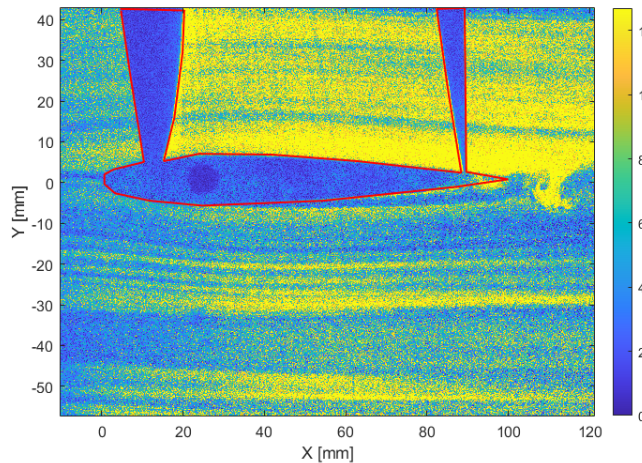


**FIGURE 3-2** 20<sup>th</sup> TIFF image of  $\alpha = 0^\circ$ ,  $dt = 100 \mu\text{s}$

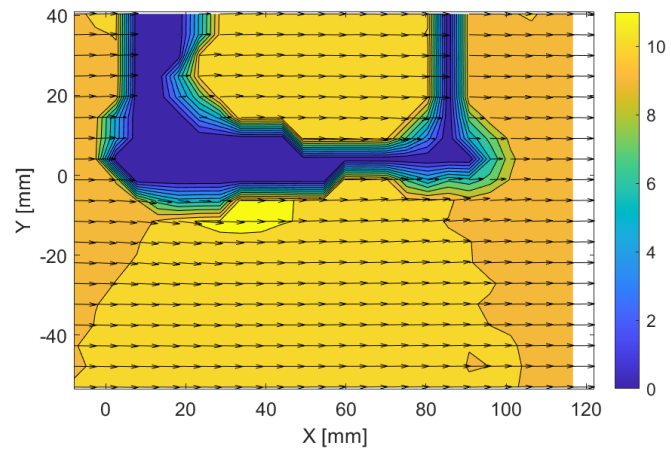


**FIGURE 3-3**  $\alpha = 0^\circ$ , 20<sup>th</sup> quiver contour plot,  $dt = 100 \mu\text{s}$ , interrogation window size = 64 pixels, 0% overlap, single pass

It is observed from Fig. 3-3 that the contours of the plot represents the airfoil inadequately and therefore this window size is not considered in further analyses where a 50% overlap and 3 multipass iterations are used in the post-processing.

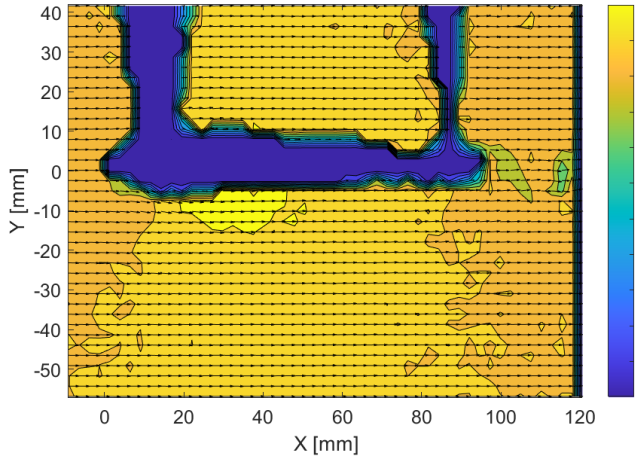


**FIGURE 3-4**  $\alpha = 0^\circ$ , 20<sup>th</sup> quiver contour plot,  $dt = 100 \mu\text{s}$ , interrogation window size = 32 pixels, 0% overlap, single pass

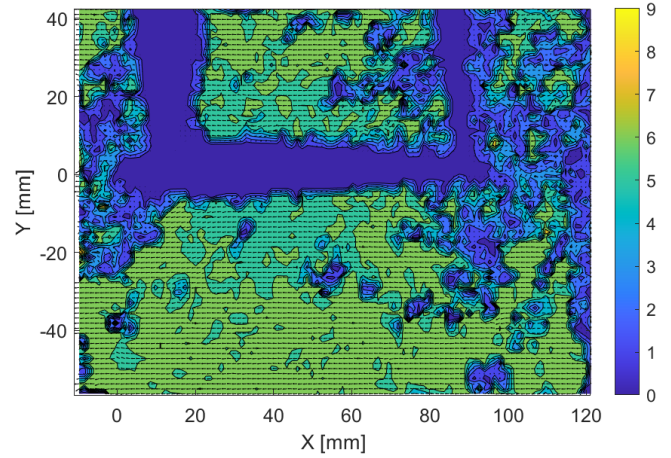


**FIGURE 3-5**  $\alpha = 0^\circ$ , 10<sup>th</sup> quiver contour plot,  $dt = 100 \mu\text{s}$ , interrogation window size = 16 pixels, 0% overlap, single pass

As for Fig. 3-4, the contour plots represents the airfoil and the flow around it considerably well compared to Fig. 3-3 and is thus considered for further analysis. Based on the circumstances of retrieving Fig. 3-5, an interrogation window of 16 pixels is not considered for further analysis as the MATLAB program fails to execute beyond the 10<sup>th</sup> image. Moreover, an extremely noisy contour plot together with freestream velocity magnitude that is far below expectation can be observed. Thus, the plot for the given parameters do not represent the flow well.

$\alpha = 5^\circ$  analysis The same set of images are presented for  $\alpha = 5^\circ$  as it was done for  $\alpha = 0^\circ$  based on the provided TIFF images as shown in Fig 3-6, where the 20<sup>th</sup> image is presented as an example. For the window size of 16 pixels, the MATLAB program once again runs into error beyond the 3<sup>rd</sup> image and thus the 3<sup>rd</sup> image has been presented instead of the 20<sup>th</sup>.

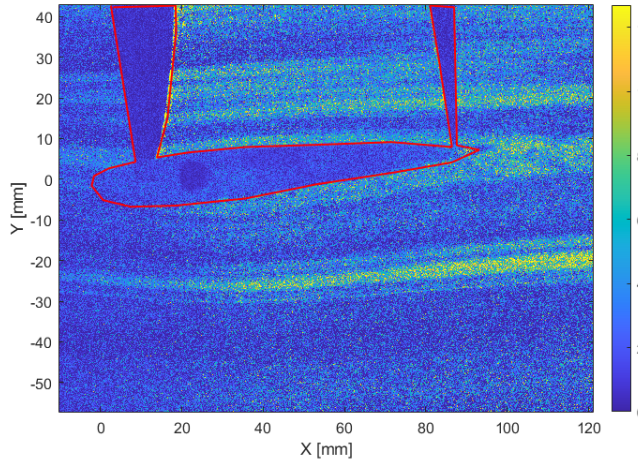


FIGURE 3-6 20<sup>th</sup> TIFF image of  $\alpha = 5^\circ$ ,  $dt = 100 \mu\text{s}$

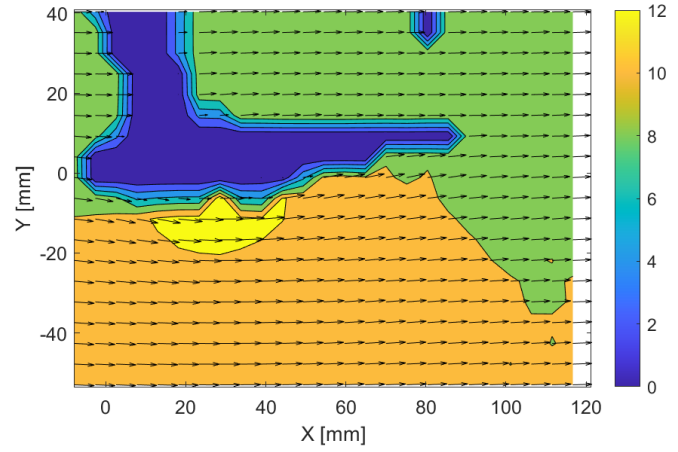


FIGURE 3-7  $\alpha = 5^\circ$ , 20<sup>th</sup> quiver contour plot,  $dt = 100 \mu\text{s}$ , interrogation window size = 64 pixels, 0% overlap, single pass

The plot that corresponds to window size of 64 pixels (Fig. 3-7) fails to represent the flow characteristics around the airfoil as the structure of the airfoil itself is missing. It is thus not considered for further analysis.

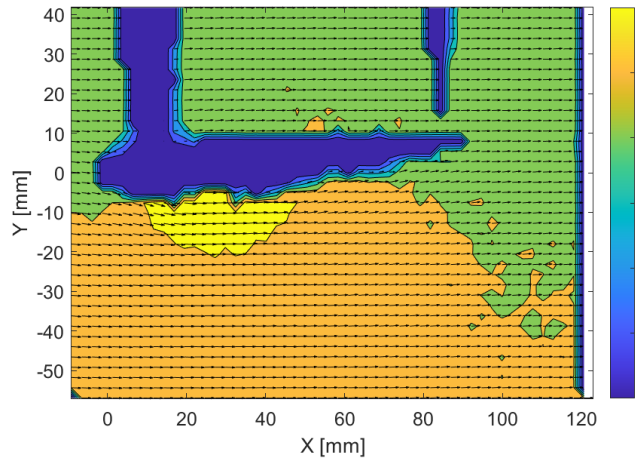


FIGURE 3-8  $\alpha = 5^\circ$ , 20<sup>th</sup> quiver contour plot,  $dt = 100 \mu\text{s}$ , interrogation window size = 32 pixels, 0% overlap, single pass

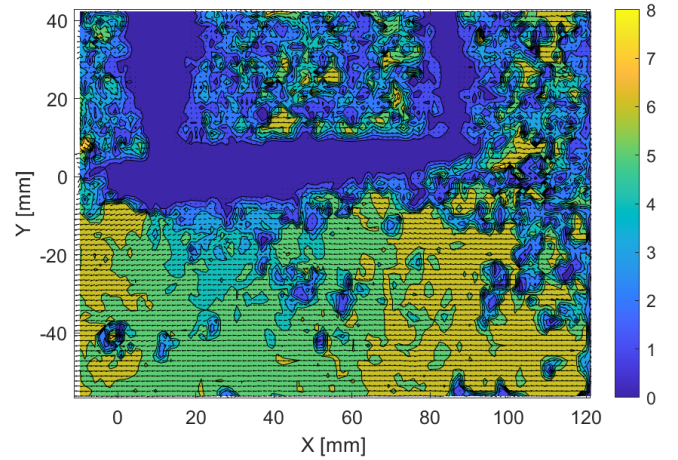
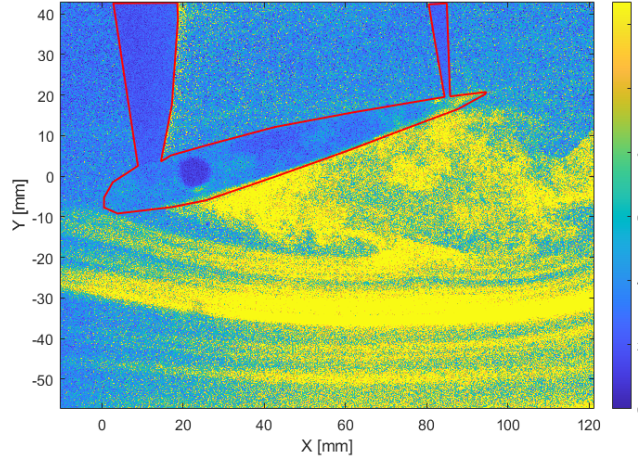


FIGURE 3-9  $\alpha = 5^\circ$ , 3<sup>rd</sup> quiver contour plot,  $dt = 100 \mu\text{s}$ , interrogation window size = 16 pixels, 0% overlap, single pass

The plot for window size of 32 as shown in Fig. 3-8 adequately describes the flow around the airfoil with magnitudes of the freestream velocity in a acceptable range and is thus considered for further analysis. Figure 3-9 shows a well-resolved airfoil structure but the flow in the domain has high noise and is also only the 3<sup>rd</sup> image due to the MATLAB program running into error beyond

this image. Furthermore, unlike the plot for window size of 32, this image shows magnitudes of the freestream velocity that are too small. Hence, it is not considered for further analysis.

**$\alpha = 15^\circ$  analysis** Lastly for  $\alpha = 15^\circ$ , the same set of figures have been produced and presented based on the provided TIFF images with an example shown in Fig. 3-10. One main difference is that instead of 20 images, 100 images were available and used for the plots.



**FIGURE 3-10** 100<sup>th</sup> TIFF image of  $\alpha = 15^\circ$ ,  $dt = 100 \mu\text{s}$

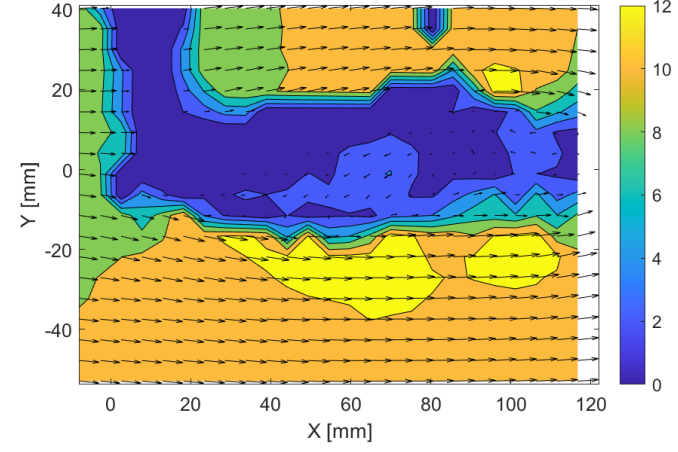


**FIGURE 3-11**  $\alpha = 15^\circ$ , 100<sup>th</sup> quiver contour plot,  $dt = 100 \mu\text{s}$ , interrogation window size = 64 pixels, 0% overlap, single pass

Unlike plots of the other values of  $\alpha$ , Fig. 3-11 represents the airfoil structure well enough but the quivers representing the flow direction are too coarsely distributed to provide meaningful discussion and thus a finer grid is required.

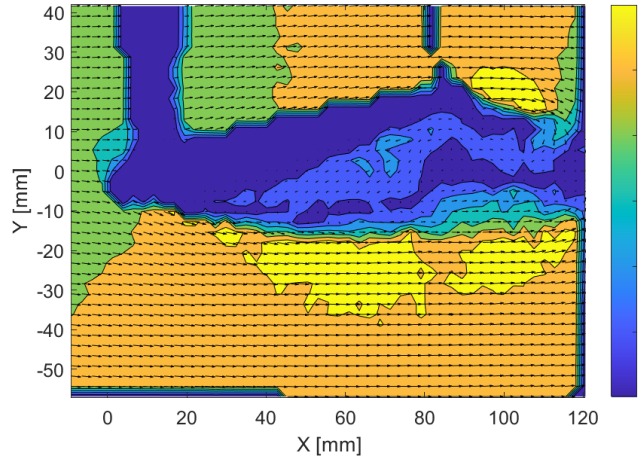


**FIGURE 3-12**  $\alpha = 15^\circ$ , 100<sup>th</sup> quiver contour plot,  $dt = 100 \mu\text{s}$ , interrogation window size = 32 pixels, 0% overlap, single pass

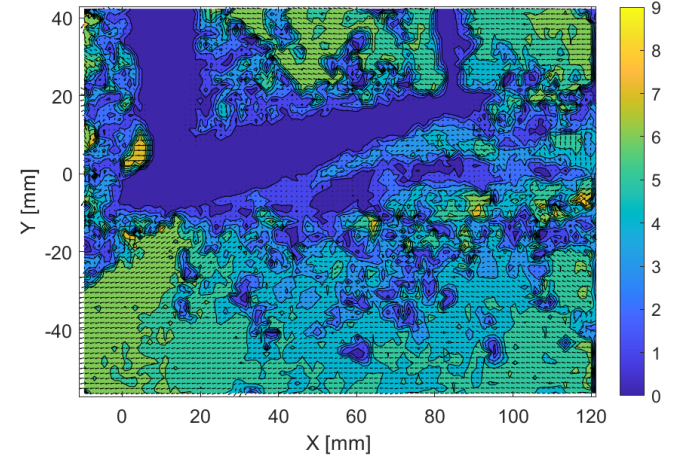


**FIGURE 3-13**  $\alpha = 15^\circ$ , 9<sup>th</sup> quiver contour plot,  $dt = 100 \mu\text{s}$ , interrogation window size = 16 pixels, 0% overlap, single pass

The plot for a window size of 32 pixels as shown in Fig. 3-12 adequately represents the airfoil and the surrounding flow with sufficient resolution. Hence, this will be considered for further

analysis. In contrast, the high flow field noise that exists in Fig. 3-13 together with small freestream velocities prevents any meaningful discussion, therefore an interrogation window size of 16 pixels will not be considered for further analysis.

In conclusion, a window size of 32 pixels is chosen for all values of  $\alpha$  for the next stage of analysis.

### 3.2.2 50% overlap and 3 multipass iterations and comparison with the self-made code

With the chosen window size of 32 pixels, the values of overlap and multipass are increased to 50% and 3 iterations respectively, up from 0% and 1 iteration in the previous section. The same type of quiver contour plots are produced for  $\alpha = 0^\circ$ ,  $5^\circ$  and  $15^\circ$  as shown in Fig. 3-14, Fig. 3-15 and Fig. 3-16 respectively. Furthermore, plots for  $dt = 6 \mu\text{s}$  have been produced for  $\alpha = 15^\circ$  and are presented in Fig. 3-17.

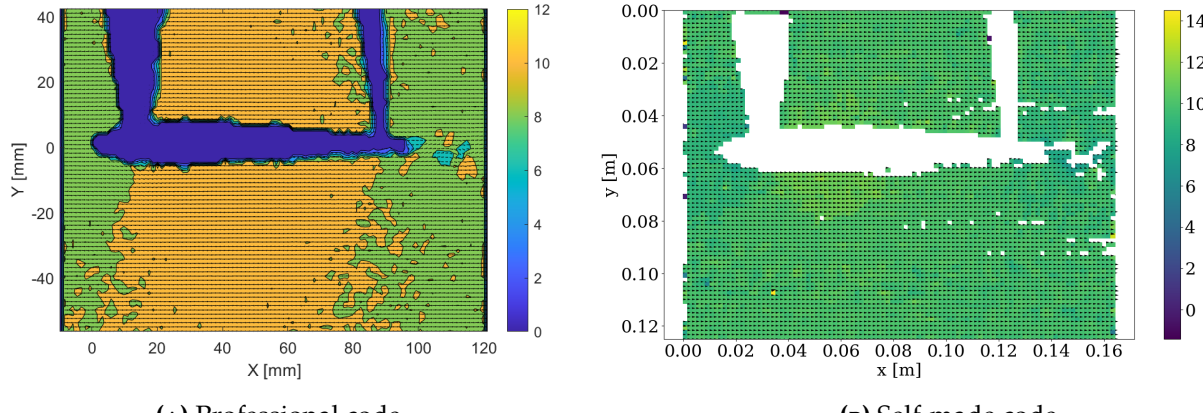


**FIGURE 3-14** Comparison of PIV-results between the professional and self-made code for  $\alpha = 0^\circ$ , 20<sup>th</sup> quiver contour plot,  $dt = 100 \mu\text{s}$ , interrogation window size = 32 pixels, 50% overlap

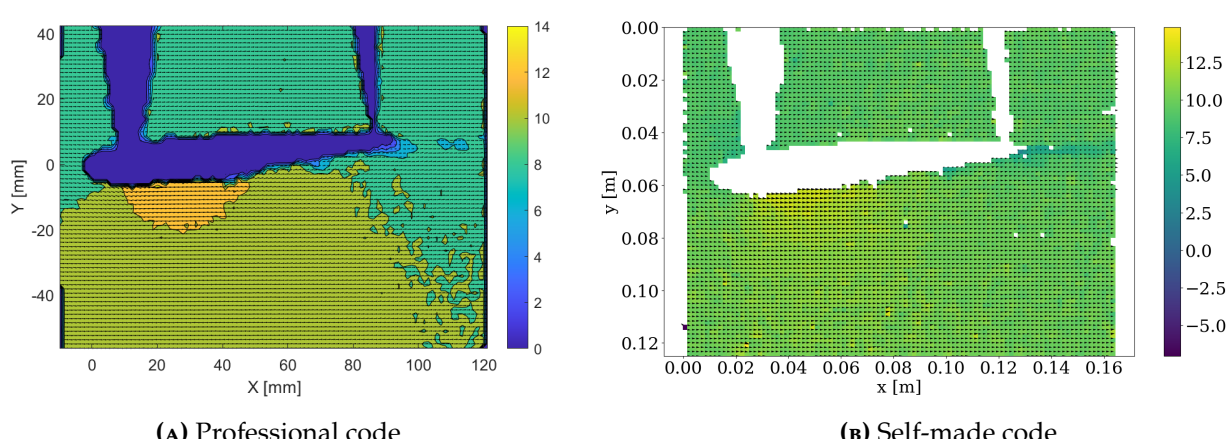


**FIGURE 3-15** Comparison of PIV-results between the professional and self-made code for  $\alpha = 5^\circ$ , 20<sup>th</sup> quiver contour plot,  $dt = 100 \mu\text{s}$ , interrogation window size = 32 pixels, 50% overlap

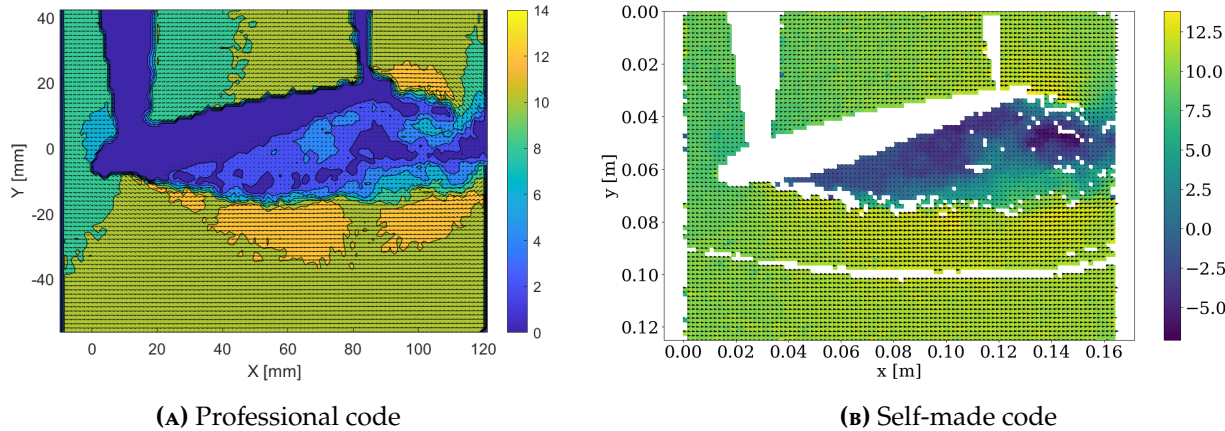


**FIGURE 3-16** Comparison of PIV-results between the professional and self-made code for  $\alpha = 15^\circ$ , 100<sup>th</sup> quiver contour plot,  $dt = 100 \mu\text{s}$ , interrogation window size = 32 pixels, 50% overlap

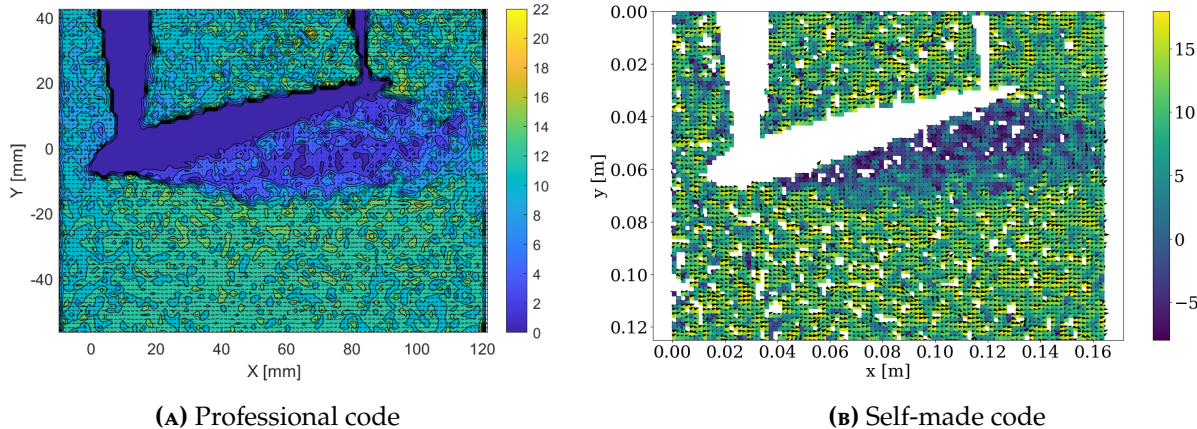


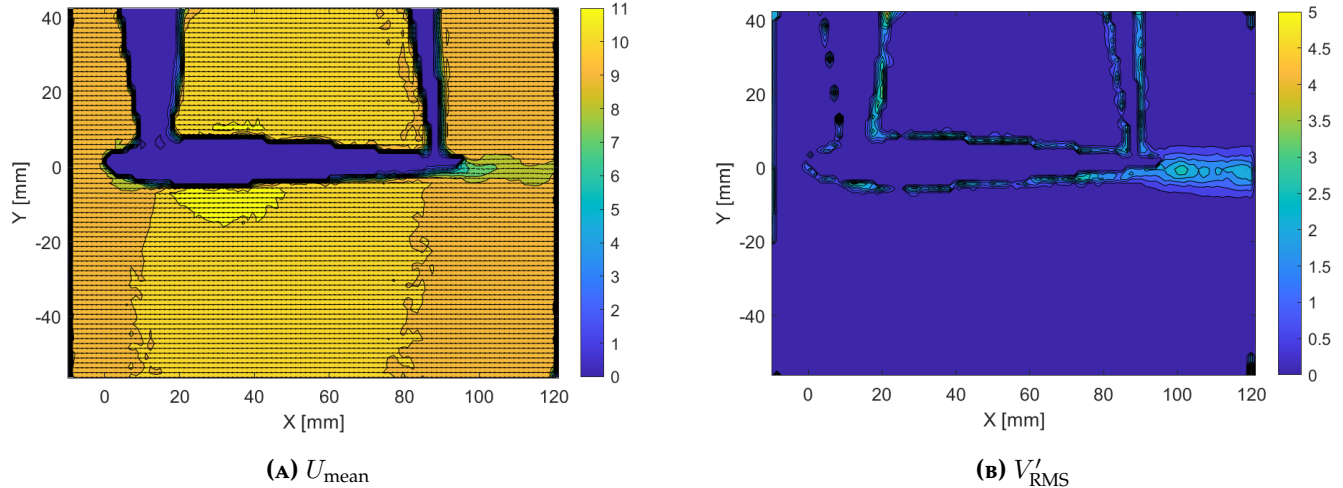
**FIGURE 3-17** Comparison of PIV-results between the professional and self-made code for  $\alpha = 15^\circ$ , 20<sup>th</sup> quiver contour plot,  $dt = 6 \mu\text{s}$ , interrogation window size = 32 pixels, 50% overlap

From the figures it can be seen that the self-made code reproduces the results of the professional code quite well. However the self-made code leaves gaps in the data where the signal-to-noise ratio is below the threshold of 1.2. An advantage of the self-made code is that it can be modified and integrated into other self-made codes quite easily.

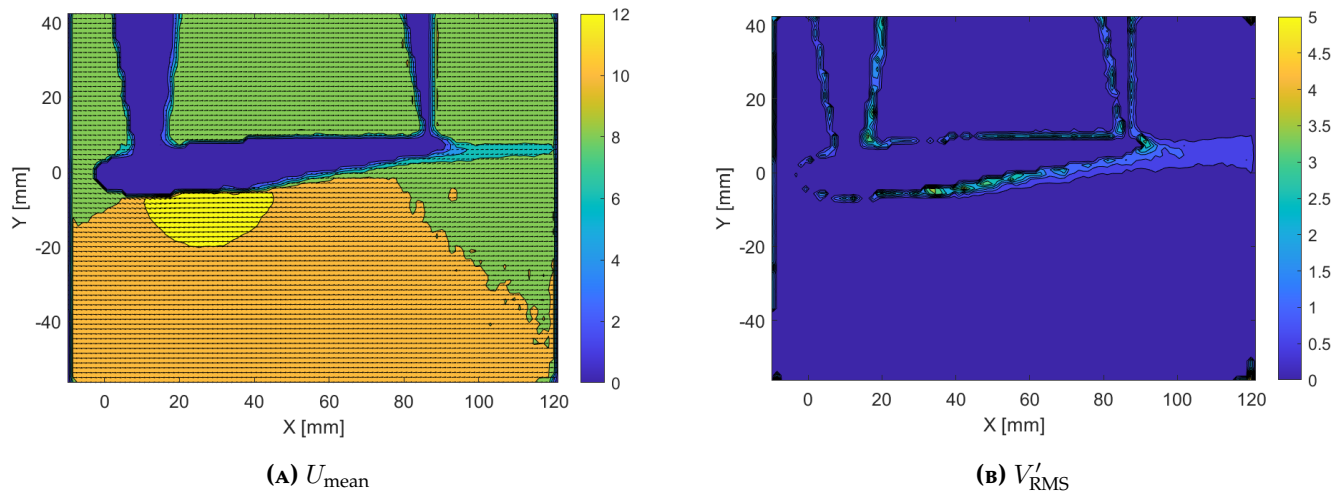
### 3.2.3 Velocity statistics

The velocity statistics of all values of  $\alpha$  have been computed using the `Stat.m` MATLAB file and the values of velocity mean and fluctuations have been computed using MATLAB functions `mean(·)` and `std(·)`. The program is then executed to produce plots of the mean  $x$ -velocity  $U_{\text{mean}}$  and flow velocity root-mean-square fluctuations  $V'_{\text{RMS}}$  (includes contributions of both  $x$ - and  $y$ -fluctuations). As for  $\alpha = 15^\circ$ , the velocity statistics have been computed using two different samples sizes: 10 and 100. Furthermore, an additional program has been produced to retrieve the velocity profile at  $x/c = 1.2$  such that the data from HWA can be compared to.

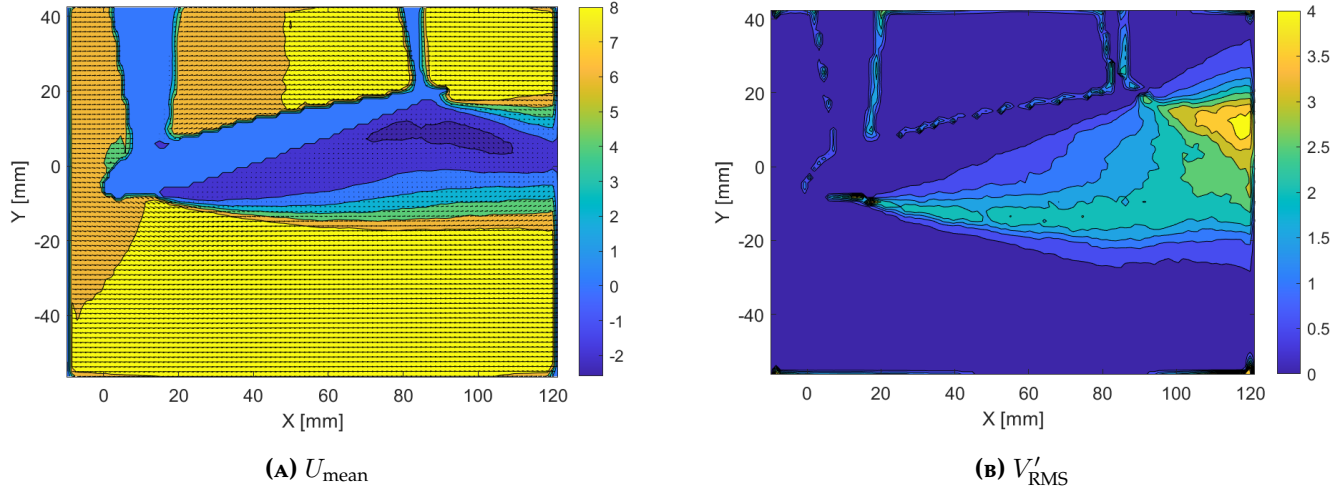
**Velocity contour plots** The velocity vector plots are produced in pairs per set of parameters:  $U_{\text{mean}}$  and  $V'_{\text{RMS}}$  and they are presented from Fig. 3-18a till Fig. 3-22b.



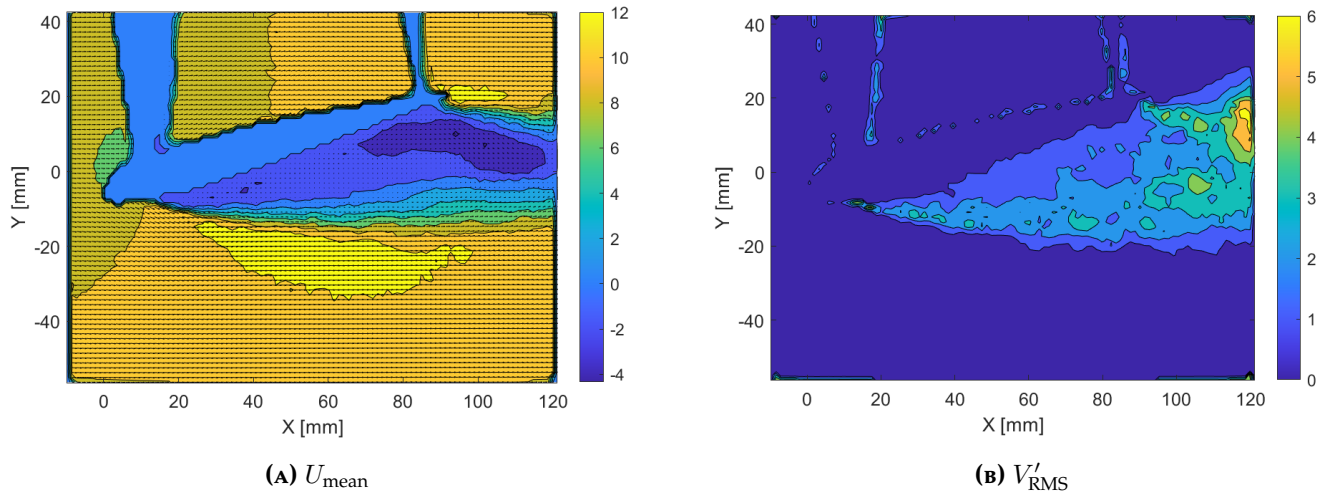
**FIGURE 3-18** Velocity plots of  $\alpha = 0^\circ$ ,  $dt = 100 \mu\text{s}$ , interrogation window size = 32 pixels, 50% overlap, triple pass



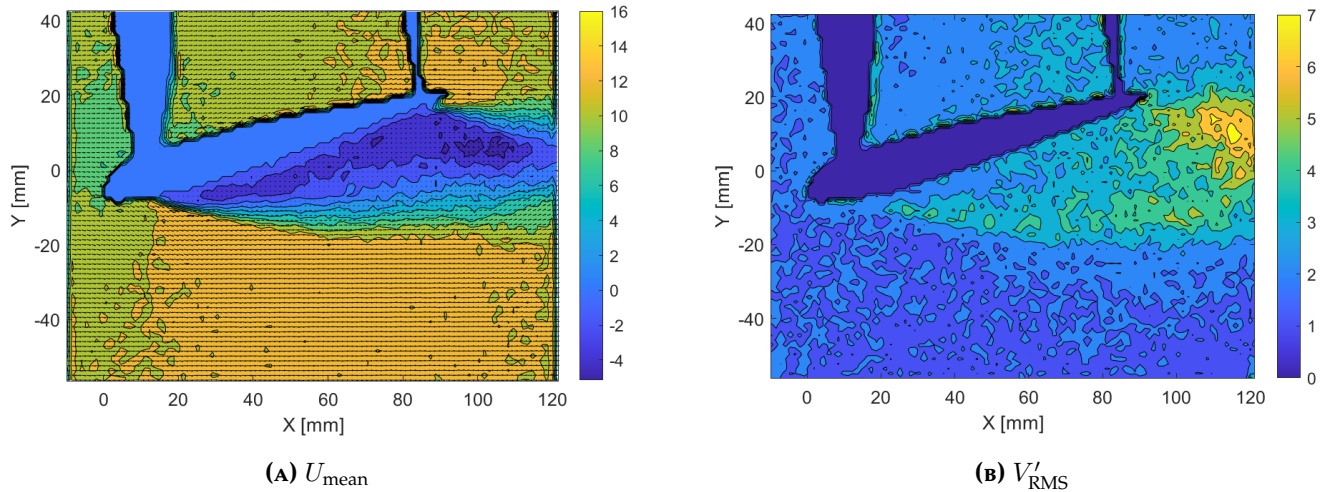
**FIGURE 3-19** Velocity plots of  $\alpha = 5^\circ$ ,  $dt = 100 \mu\text{s}$ , interrogation window size = 32 pixels, 50% overlap, triple pass



**FIGURE 3-20** Velocity plots of  $\alpha = 15^\circ$ ,  $dt = 100 \mu\text{s}$ , interrogation window size = 32 pixels, 50% overlap, triple pass, 100 samples



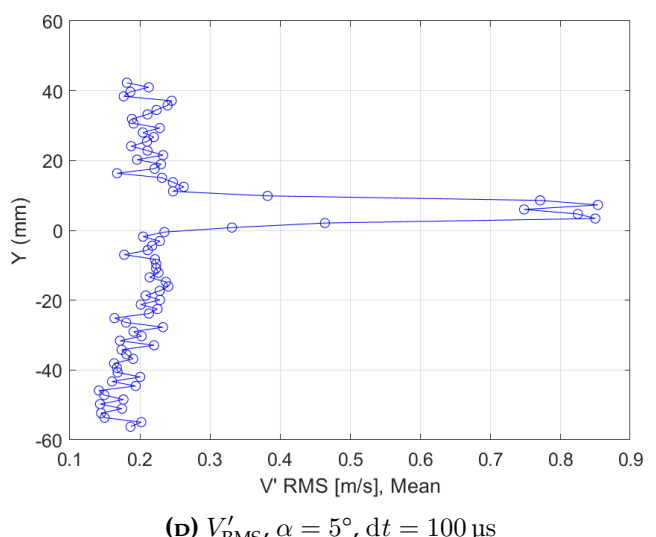
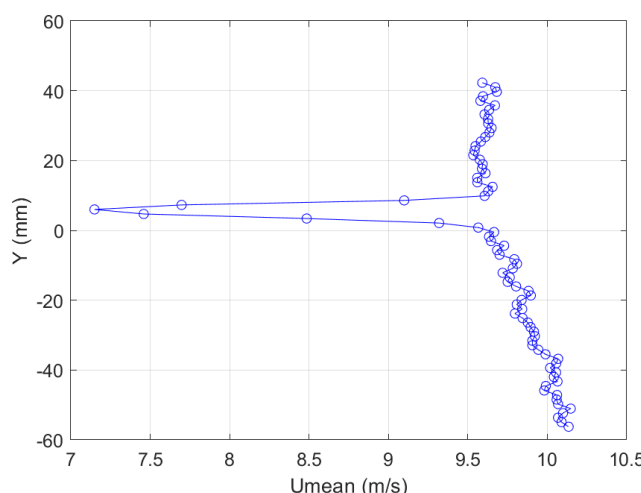
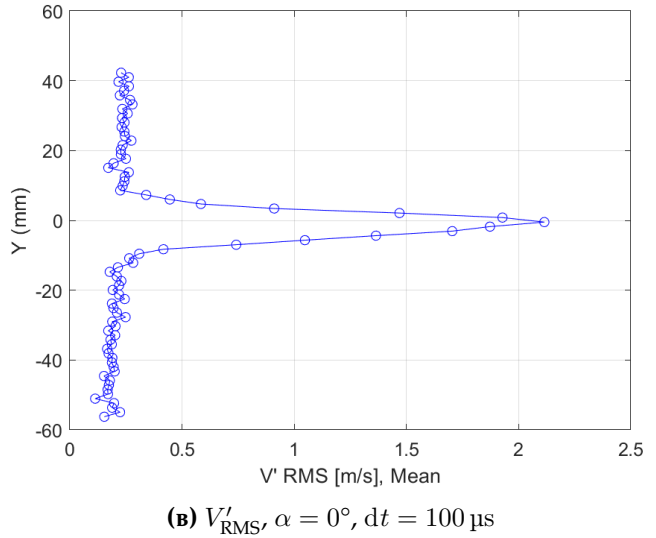
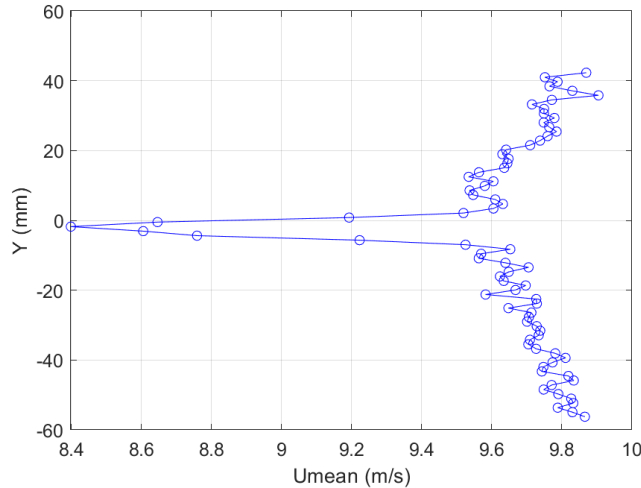
**FIGURE 3-21** Velocity plots of  $\alpha = 15^\circ$ ,  $dt = 100 \mu\text{s}$ , interrogation window size = 32 pixels, 50% overlap, triple pass, 10 samples

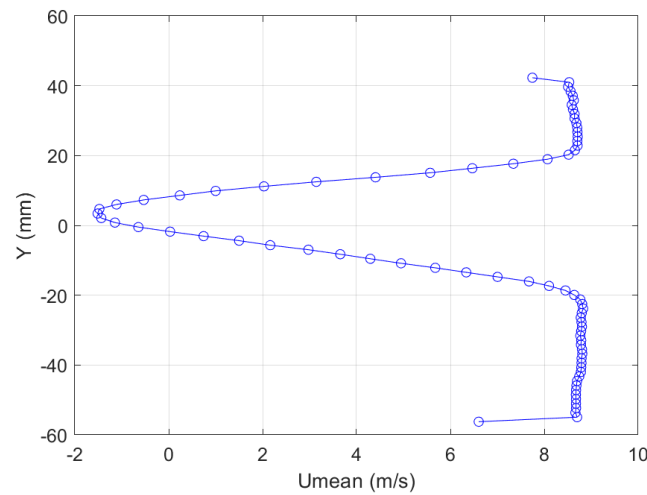
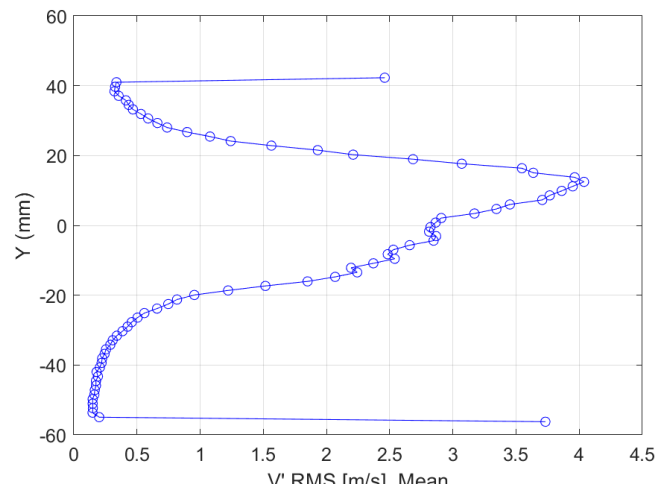
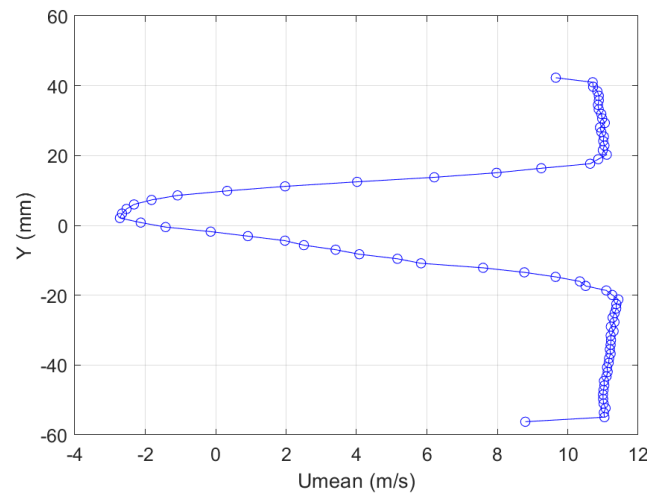
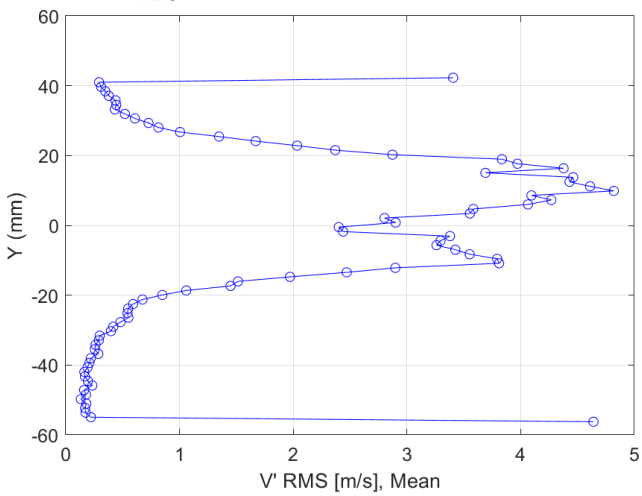
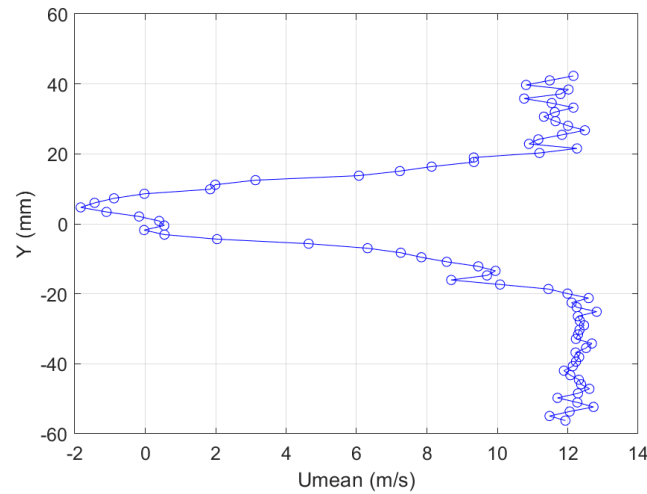
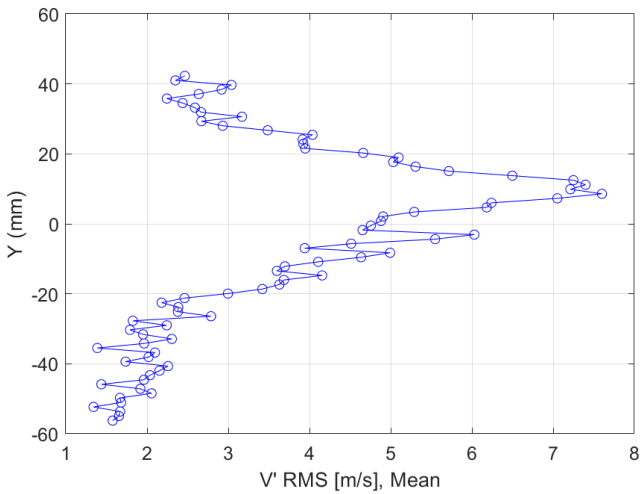


**FIGURE 3-22** Velocity plots of  $\alpha = 15^\circ$ ,  $dt = 6 \mu\text{s}$ , interrogation window size = 32 pixels, 50% overlap, triple pass

It is observed that at higher angles of attack, large fluctuation regions appear on the airfoil's suction side. The large fluctuation magnitudes strongly suggests that a (near) steady-state solution does not exist within the separation zone. The reasoning behind this statement is that since  $U_{\text{mean}}$  is effectively derived from a time-averaging operation, the velocity field represents a time-independent solution. The fluctuations represent the deviations from this time-independent solution, and large deviations imply poor representation by a time-averaged field.

**Velocity profile at  $x/c = 1.2$**  The  $x/c = 1.2$  velocity profile plots for  $U_{\text{mean}}$ . These are presented from Fig. 3-23a till Fig. 3-23i.  $V'_{\text{RMS}}$  has also been plotted at  $x/c = 1.2$  and presented from Fig. 3-23b till Fig. 3-23j. They seem to reflect the behavior of  $U_{\text{mean}}$  well at the given location of  $x/c = 1.2$  as it can be observed that for a higher angle of attack, the region of smaller velocities is larger and this represents the fluctuations on the suction side. Ultimately, they will be compared against the HWA counterparts at the end of the section.



(e)  $U_{\text{mean}}, \alpha = 15^\circ, dt = 100 \mu\text{s}, 100 \text{ samples}$ (f)  $V'_{\text{RMS}}, \alpha = 15^\circ, dt = 100 \mu\text{s}, 100 \text{ samples}$ (g)  $U_{\text{mean}}, \alpha = 15^\circ, dt = 100 \mu\text{s}, 10 \text{ samples}$ (h)  $V'_{\text{RMS}}, \alpha = 15^\circ, dt = 100 \mu\text{s}, 10 \text{ samples}$ (i)  $U_{\text{mean}}, \alpha = 6^\circ, dt = 100 \mu\text{s}$ (j)  $V'_{\text{RMS}}, \alpha = 6^\circ, dt = 100 \mu\text{s}$ 

**FIGURE 3-23** Velocity profile plots at  $x/c = 1.2$ , interrogation window size = 32 pixels, 50% overlap, triple pass

### 3.3 Instantaneous and mean flow comparison

The instantaneous and mean velocity fields are investigated in this section. For convenience, the instantaneous and mean field graphs for each  $\alpha$  are shown adjacent to each other below. Between Fig. 3-14a and Fig. 3-18a, it becomes evident that the instantaneous field is similar to the mean field. The wake that forms in the instantaneous field roughly reflects the wake that is seen in the mean field. The fluctuations in the field are easily visualized in the instantaneous field, where there are no smooth contours present.

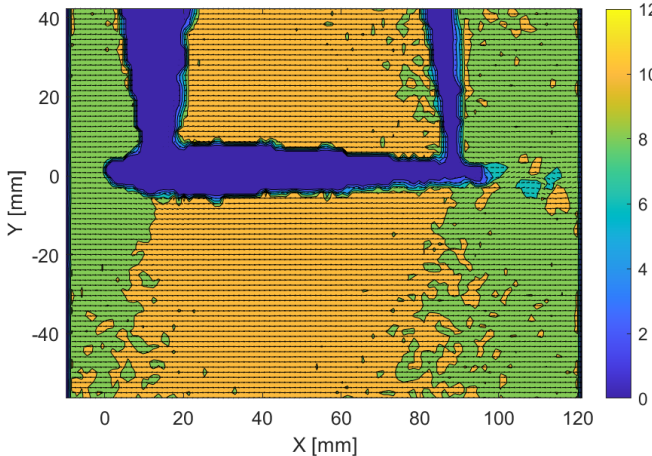


**FIGURE 3-14A** Professional PIV-results for  $\alpha = 0^\circ$ , 20<sup>th</sup> quiver contour plot,  $dt = 100 \mu\text{s}$ , interrogation window size = 32 pixels, 50% overlap (repeated from page 19)

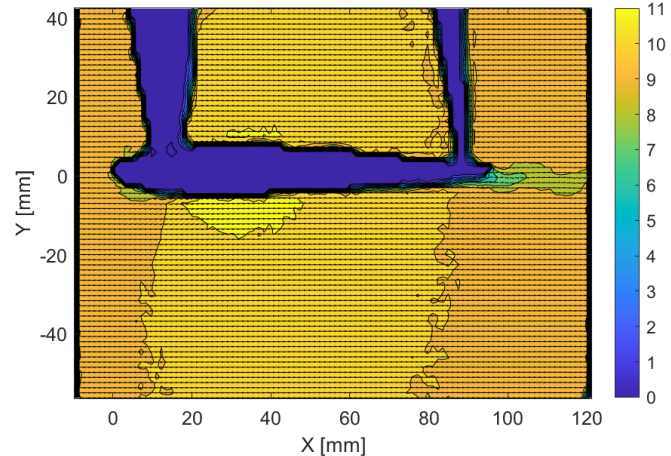


**FIGURE 3-18A**  $U_{\text{mean}}$  contour plot of  $\alpha = 0^\circ$ ,  $dt = 100 \mu\text{s}$ , interrogation window size = 32 pixels, 50% overlap, triple pass (repeated from page 21)

Between Fig. 3-15a and Fig. 3-19a, similar arguments are made as to the ones made for  $\alpha = 0^\circ$ . The primary observation is that the wake is larger in the mean flow, and that exists zones of low velocity attached to the airfoil. The larger wake zone and the low velocity regions attached to the airfoil suggests flow separation, but no support is made for this statement. It is likely that this low velocity region is an artifact of the post-processing method used.

Between Fig. 3-16a and Fig. 3-20a, the main difference is in the separation that stems near the leading edge. It is evident that the instantaneous separation zone is more irregular than the mean separation zone – both internally and on the boundary. Internally, the instantaneous zone shows large variations in velocity, whereas the mean field completely smoothens out these variations. Similarly for the boundary of the separation zone, the instantaneous zone contains rough contours, whereas the mean field exhibits smooth contours throughout the domain due to the averaging process.

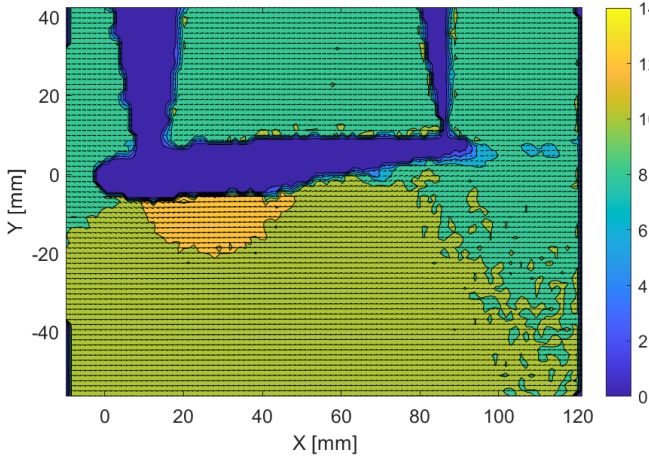


**FIGURE 3-15A** Professional PIV-results for  $\alpha = 5^\circ$ , 20<sup>th</sup> quiver contour plot,  $dt = 100 \mu\text{s}$ , interrogation window size = 32 pixels, 50% overlap (repeated from page 19)

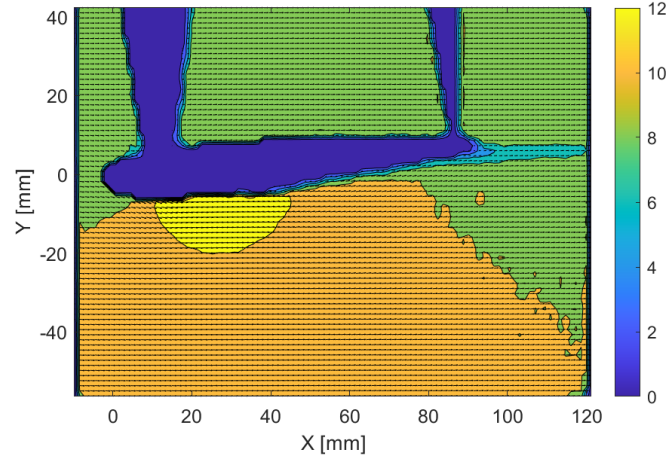


**FIGURE 3-19A**  $U_{\text{mean}}$  contour plot of  $\alpha = 5^\circ$ ,  $dt = 100 \mu\text{s}$ , interrogation window size = 32 pixels, 50% overlap, triple pass (repeated from page 21)

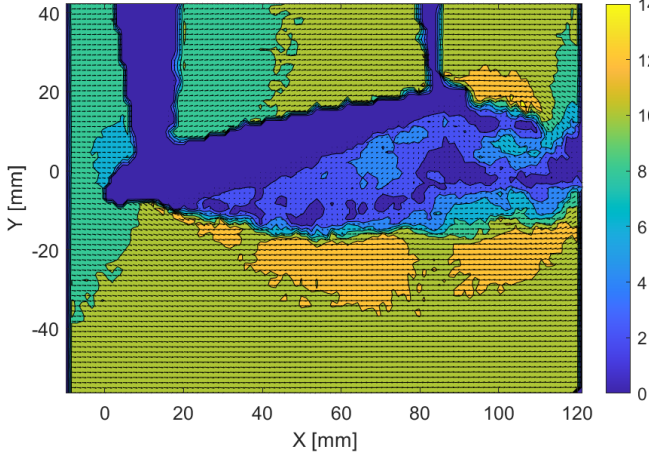


**FIGURE 3-16A** Professional PIV-results for  $\alpha = 15^\circ$ , 100<sup>th</sup> quiver contour plot,  $dt = 100 \mu\text{s}$ , interrogation window size = 32 pixels, 50% overlap (repeated from page 20)

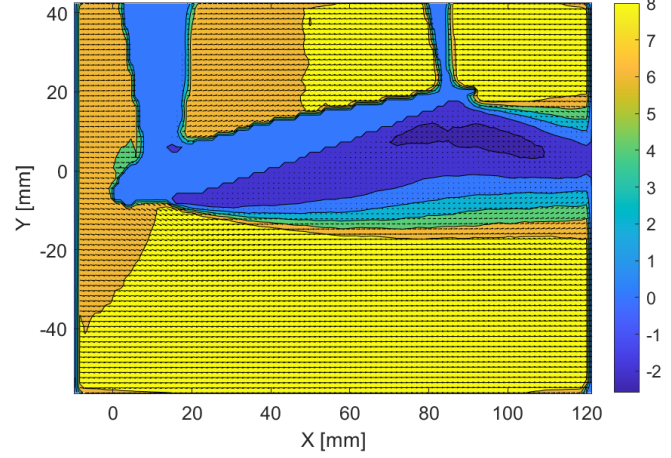


**FIGURE 3-20A**  $U_{\text{mean}}$  contour plot of  $\alpha = 15^\circ$ ,  $dt = 100 \mu\text{s}$ , interrogation window size = 32 pixels, 50% overlap, triple pass, 100 samples (repeated from page 22)

## 3.4 Comparison of HWA and PIV

The mean velocity profiles and the root-mean-square fluctuations at  $x/c = 1.2$  obtained with both HWA and PIV are shown for different angles of attack in Fig. 3-24.

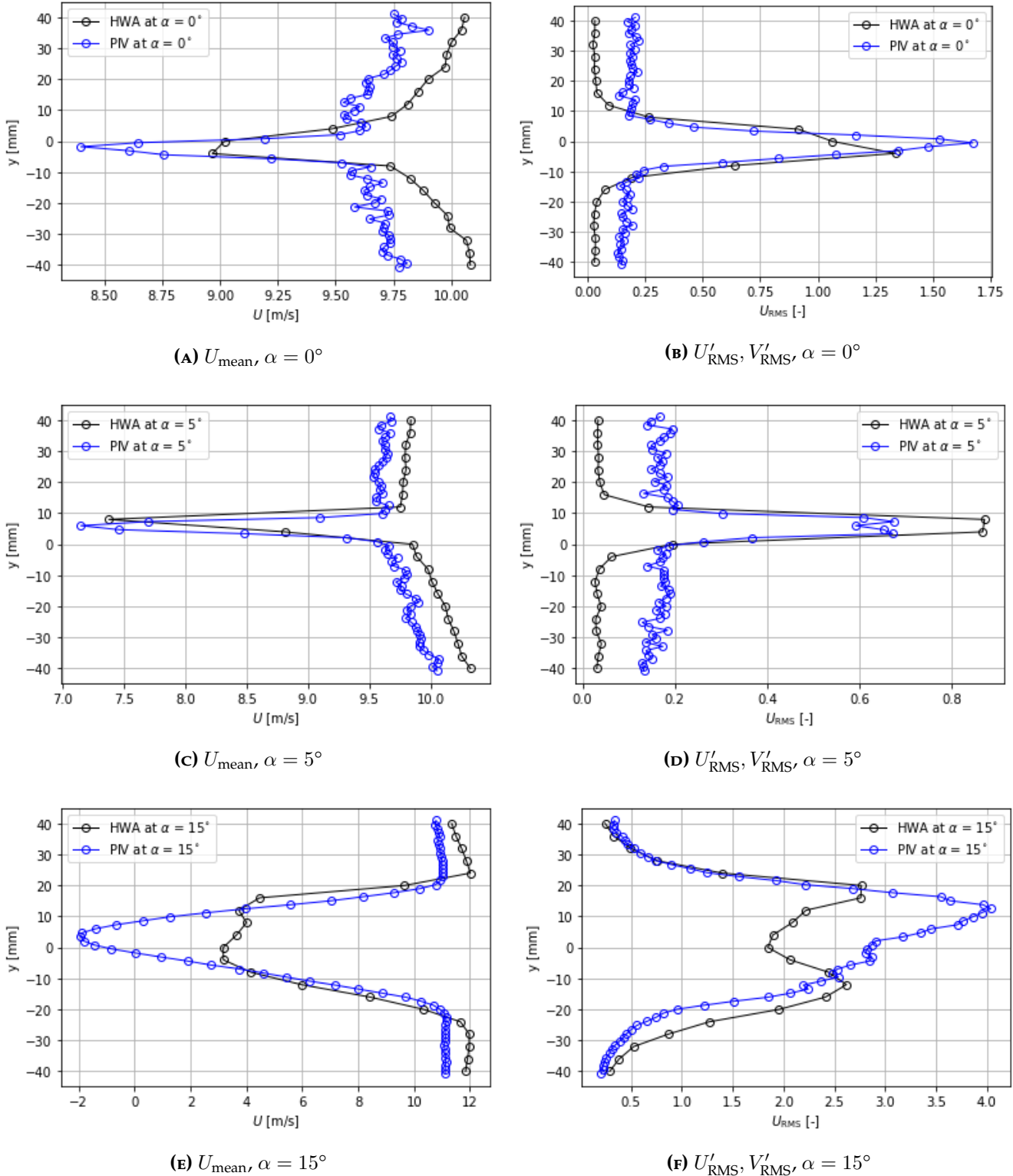


FIGURE 3-24 HWA and PIV comparison of  $U_{\text{mean}}$  and  $U'_{\text{RMS}}, V'_{\text{RMS}}$  at different  $\alpha$

It can be seen that the general shape of the profile matches for the two lower angles of attack,  $\alpha = 0^\circ$ , and  $\alpha = 5^\circ$ . However, for  $\alpha = 15^\circ$ , the highest angle of attack, the profile is truncated in the region of the centerline ( $y = 0$  mm). This is due to the limitations of HWA in reversed flows, as only magnitudes of the flow velocity can be measured. Additionally, the  $y$ -component of

velocity influences the measured velocity by HWA. Furthermore, the mean velocity measured by PIV is lower than the mean velocity measured in comparison to HWA in the freestream regions. In contrast to this, the RMS-fluctuations are higher for the PIV measurements for the two lowest angles of attack. This occurs as the PIV measurements considers the fluctuations of both velocity components,  $x-$  and  $y-$ , while HWA includes only the fluctuations in the  $x-$ velocity component. Therefore the net contribution is higher for PIV than it is for HWA.

In general, the advantage of PIV against HWA is that instantaneous velocity profiles and two-dimensional profiles can be measured. PIV also provides directional velocity data in contrast to HWA. This can be remedied by using up to three wires at an angle to each other. While PIV is a less intrusive measurement technique, it is also more expensive in terms of needed equipment and data analysis software. The maximum sampling rate of HWA is also higher than is possible with PIV measurements.

# 4 Conclusion

The flow around a NACA 0012 airfoil was measured at three different angles of attack using particle image velocimetry (PIV) and hot wire anemometry (HWA). The results of the PIV dataset were analyzed using a provided professional code and a self-made code that was developed in Python during the course. The results from both tools were compared for instantaneous flowfields. The comparison showed good agreement in the flow structure and the magnitude of measured velocities between the two tools. The self-made code however had data gaps present in the result due to the high signal-to-noise ratio threshold, which is a trade-off made when comparing it to the professional code. However the self-made code is able to be modified and implemented into other workflows more easily than the provided professional code.

The HWA data was calibrated using a 4<sup>th</sup> order polynomial following from King's Law. From the HWA data, the mean  $x$ -velocity and root mean squared (RMS)  $x$ -velocity fluctuations could be measured along a vertical axis located at 20% of the airfoil's chord behind its trailing edge. The obtained velocity profiles were compared to data extracted from the PIV measurements. It was found that the two methods compared reasonably well, with small discrepancies in the freestream velocity present. However, the profiles in the wake of the airfoil at an angle of attack of 15 degrees did not match, which is due to limitations of the HWA measurement technique.

# Works Cited

- [1] A. Sciacchitano et al. *Flow Measurement Techniques – Student Manual for the Laboratory Exercise (AE4-180)*. Student Manual. Delft University of Technology, Delft, South Holland, 2628 CD: Delft University of Technology, Apr. 2021.
- [2] Mark J. Tummers. "Investigation of a turbulent wake in an adverse pressure gradient using Laser Doppler Anemometry." PhD thesis. Delft, South Holland, 2628 CD: Delft University of Technology, Nov. 1999.
- [3] Sagar Adatrao, Michele Bertone, and Andrea Sciacchitano. "Multi- $\Delta t$  approach for peak-locking error correction and uncertainty quantification in PIV." In: *Measurement Science and Technology* 32.5 (Mar. 2021), p. 054003. doi: 10.1088/1361-6501/abdcde. URL: <https://doi.org/10.1088/1361-6501/abdcde>.